Research Square

Preprints are preliminary reports that have not undergone peer review.
They should not be considered conclusive, used to inform clinical practice,
or referenced by the media as validated information.

Memristive Motion-Streak Neuron for Spatiotemporal Multiple Object Detection

Cheol Seong Hwang

cheolsh@snu.ac.kr

Seoul National University https://orcid.org/0000-0002-6254-9758

Hyungjun Park

Seoul National University

Jin Hong Kim

Seoul National University

Hyun Wook Kim

Seoul National University

Néstor Ghenzi

Seoul National University

Sung Keun Shim

Seoul National University

Joon-Kyu Han

Seoul National University https://orcid.org/0000-0002-8736-9091

Min Chung Jung

Seoul National University

Dong Hoon Shin

Seoul National University

Kyung Seok Woo

Ulsan National Institute of Science and Technology https://orcid.org/0000-0001-9184-7255

Article

Keywords: neuromorphic computing, optoelectronic memristor, dynamic memristor, motion streak neuron, dynamic vision sensor, spatiotemporal processing

Posted Date: March 18th, 2026

DOI: https://doi.org/10.21203/rs.3.rs-8957622/v1

License: This work is licensed under a Creative Commons Attribution 4.0 International License.
Read Full License

Additional Declarations: There is **NO** Competing Interest.

Abstract

Conventional artificial vision systems process dynamic scenes inefficiently by reconstructing motion from discrete frames, a process that requires post-processing. In contrast, real-world environments containing multiple moving objects demand sensor-level discrimination. This work presents a memristive motion-streak neuron that performs spatiotemporal encoding by integrating an Al/InGaZnO/Al optomemristor with an Ag/HfO2/Pt dynamic memristor, whose relaxation dynamics provide temporal memory. In this system, the presence time of moving objects is detected by decay of the output current, allowing motion direction and speed to be directly inferred from the relaxation behavior. The integrated memristor pixel array enables processing of continuous movements and achieves 96.2% classification accuracy for multiple objects. Also, integrating the motion-streak neuron with the resistor–capacitor kernel further encodes temporal intervals between optical events, enabling recognition of complex movement patterns. This event-driven processing diminishes computational overhead and provides a hardware solution for next-generation vision systems.

Main

Recent advancements in artificial intelligence significantly improved machine vision performance by mimicking biological vision systems[1–5]. However, most machine vision systems are predominantly designed for static image perception through a frame-by-frame approach rather than continuous dynamic scenes[6-8], resulting in redundant data transfer and high latency, particularly when multiple objects move simultaneously at different speeds and in different directions. Therefore, dynamic vision systems capable of simultaneously analyzing spatiotemporal information are crucial for efficiently handling massive video data[9].

The biological visual system does not reconstruct dynamic scenes from discrete frames[10,11], but it integrates dynamic visual inputs as a continuous stream by overlaying image frames to form a single, integrated visual scene, thereby enabling perception of complex visual scenarios[12-14]. A key component of this spatiotemporal integration is a motion-streak neuron that combines successive visual inputs into residual traces of moving objects, enabling the processing of continuous visual data and rapid motion perception. Inspired by this principle, neuromorphic memristive motion detection and perception systems require elements that simultaneously exhibit stimulus responsiveness and intrinsic dynamic memory to encode complex motion features directly within the device.

This work introduces a memristive motion-streak neuron by integrating an Al/InGaZnO (IGZO)/Al optomemristor with an Ag/HfO_2/Pt dynamic memristor, forming a unit that functions as an individual pixel and captures spatiotemporal data from multiple objects. The integrated memristor pixel (neuron) enables learning from video data using a single embedded frame, without processing each frame individually. A 4 × 4 motion-streak neuron array was fabricated, and its operational principle was confirmed by illuminating the devices with laser pulses of controlled direction and speed (duration). Subsequently, the KTH dataset was simulated to demonstrate that the integrated system can accurately

recognize the direction and speed of multiple moving objects, comparable to existing software solutions[15,16]. Furthermore, integration with a resistor–capacitor (R–C) kernel allows the proposed neuron to detect complex motion of multiple objects, supporting scalable motion-processing applications. This study presents a method that bridges the gap between artificial and biological vision systems.

Motion streak neuron with dynamic relaxation for spatiotemporal multiple object detection

Figure 1a illustrates how the motion-streak neurons in the human cerebral cortex integrate temporal frames from multiple objects into a single visual frame, where multiple frames were combined to form residual traces to infer the speed and direction of moving objects[17]. Direction is determined by the object's position in the final embedded frame relative to its residual trace. Also, speed is characterized by the length of these traces; fast- and slower-moving objects leave shorter and longer traces, respectively[18].

Figure 1b presents an implementation of a memristive motion-streak neuron composed of Al/InGaZnO/Al optoelectronic memristors and Ag/HfO_2/Pt dynamic memristors, emulating the biological motion-streak neuron. Light pulses activate optoelectronic memristors and primarily encode the spatial position of a moving object, while the dynamic memristors are triggered by electrical pulses and capture the object speed[19]. **Figure 1c** illustrates how distinct motion streak patterns emerge from the relaxation behavior of the dynamic memristor when light pulses are applied to the integrated device. In this method, the duration of a moving object's presence on a pixel is represented by the length of the light pulse. A fast-moving object corresponds to a short light pulse, resulting in rapid decay of the dynamic memristor current and the formation of a short motion trail. In contrast, a slow-moving object is represented by a longer light pulse, which induces a prolonged relaxation process and generates extended motion streaks.

Figure 1d presents a 4 × 4 array of motion-streak neurons with different operational principles. In a conventional frame-based approach, each light pulse is considered as a single frame, and the frames are processed independently. As a result, dynamic motion is segmented into discrete segments, and thus, objects moving at different speeds cannot be reliably distinguished. In the static approach, motion trails are observed as a function of pulse length. However, the length of the motion trail (or decay time constant) does not vary with the object presence time (or light pulse length). Therefore, object speeds cannot be distinguished when objects move simultaneously. In contrast, the proposed dynamic approach modulates the intrinsic relaxation dynamics of the dynamic memristor. Distinct motion trails are generated based on the object's presence time at each pixel: longer decay time for longer presence (or pulse application) time. Through these properties, clear and simultaneous discrimination of object identity, motion speed, and direction is achieved without additional signal processing.

Electrical and optical properties of the Ag/HfO_2/Pt dynamic memristor, Al/IGZO/Al optomemristor and the integrated device

The Ag/HfO_2/Pt dynamic memristor was investigated to emulate the temporal processing behavior of biological motion-streak neurons[20]. **Figure 2a** shows 50 cycles of current-voltage (*I-V*) characteristics of the dynamic memristor. After the forming process, the dynamic memristor exhibits abrupt volatile switching behavior below 1 V (**Supplementary Fig. 1**). When an electrical pulse was applied, the circuit exhibited a relaxation response due to the inherent parasitic capacitance of the memristor, and **Figure 2b** represents the typical relaxation behavior under a constant voltage pulse. The switching from a low-conductance state to a high-conductance state in the memristor is due to the formation of a silver conductive filament induced by the migration of silver cations under an electric field. When the pulse terminates, the device relaxes to a low-conductance state (volatile off-switching) via spontaneous filament rupture driven by the surface energy of the conducting filaments[21–25].

Figure 2c presents that the off-switching relaxation time varied from 1.7 ms to 2.1 ms as the applied voltage pulse length increased from 1 ms to 4 ms at a fixed pulse amplitude of 2.8 V and a serial resistor of 10 MΩ. These varying relaxation times are attributed to differences in the diameter of the silver conductive filament. **Figure 2d** shows the results as the serial resistance increases from 10 MΩ to 50 MΩ under a fixed pulse condition (2.5 ms, 2.8 V). As the serial resistance increases, the voltage across the dynamic memristor decreases, decreasing the output current and shortening the relaxation time. Therefore, the Ag/HfO_2/Pt dynamic memristor exhibits relaxation dynamics that depend on applied voltage pulse length and serial-resistor conditions. **Supplementary Figs. 2-5** shows the additional electrical characteristics of the dynamic memristor.

Figure 2e exhibits a rapid photoresponse of the Al/IGZO/Al optomemristor, with a rising time of 100 μs and a falling time of 60 μs under a light pulse with an intensity of 12.35 mW/cm^2 and a pulse length of 0.5 ms. These sub-hundred-μs responses are superior to those of previously reported oxide-based photodetectors[26–28]. The rapid photoresponse indicates that the proposed device can detect rapid visual data and convert it into electrical signals with minimal delay. **Supplementary Figs. 6 and 7** present the band diagram and temperature dependence of the optomemristor under light-on/off conditions.

Also, **Supplementary Fig. 8** confirmed the reliable performance of the optomemristor over a 1.5-s period of consecutive 2-ms light pulses. The light response originates from a reversible reaction involving the ionization (V_O à V_O^{2+} + 2e) for light on and neutralization (V_O^{2+} + 2eàV_O) for light off of an oxygen vacancy (V_O)[19]. The amorphous IGZO thin film exhibits favorable optical properties, which are attributed to numerous localized trap sites (neutral V_O). Furthermore, **Supplementary Fig. 9** represents stable light-switching endurance over 400 consecutive cycles under a 2.8 V electrical bias with successive 2 ms light pulses. **Supplementary Note 1** shows more detailed discussions about the electrical conduction mechanism of the optomemristor with and without light.

Figure 2f shows that an Al/IGZO/Al optomemristor was serially connected to the Ag/HfO_2/Pt dynamic memristor in place of the serial resistor, representing a single motion-streak neuron (pixel). **Supplementary Fig. 10** shows the schematic fabrication process flow of the integrated motion-streak

neuron. **Figure 2g** illustrates the relaxation behavior of the integrated motion-streak neuron under light-on/off conditions. At a fixed pulse (4 V, 8 ms), the relaxation time increases under illumination because the optomemristor has a lower resistance, thereby increasing the voltage across the dynamic memristor and resulting in a higher output current and longer relaxation time. **Supplementary Figs. 11** and **12** show the *I*–*V* characteristics and endurance of the integrated device, demonstrating its electrical stability.

Figure 2h demonstrates the photo-responsive characteristics, which affect both the output current and relaxation behavior. The output current and relaxation time increased under the light-on condition at all voltage pulse lengths, confirming the ability to process spatiotemporal information. The output current and relaxation time of 16 devices were measured to compare variation across the integrated devices (**Supplementary Figs. 13-15**). Previous studies on optomemristors for motion detection were limited by the static photoresponse of the active layers[29-32]. In contrast, this device can simultaneously process object motion.

Single object movement classification with integrated motion-streak neuron array

Figure 3a illustrates the custom optical board setup used to demonstrate the operation of the memristive motion-streak neuron experimentally. **Supplementary Fig. 16** shows the hardware configuration used to detect a single object moving in different directions. The Methods section and **Supplementary Note 2** provide detailed descriptions of the optical measurement setup.

To emulate the movement of a single object, optical pulse signals were applied with arbitrary directions and speeds, while a voltage of 4 V was applied simultaneously across all neuron devices. In this task, object speed was defined by the optical pulse length applied to each pixel. For example, a slow-moving object traveling to the right was implemented by applying four consecutive light pulses to the right at a rate of 3 ms per pixel, resulting in a total illumination duration of 12 ms. The direction and speed of the moving object were then determined by measuring the current responses of all motion streak neurons at the end of the 12 ms pulse sequence. **Supplementary Fig. 17** shows the light-pulse measurement system used to characterize the relaxation time of the motion-streak neuron.

Figures 3b-d present experimentally measured current values obtained from the 4 × 4 motion-streak neuron array for an object moving from the bottom left corner toward the top right corner along the diagonal direction at three different speeds. The color bar maps the current for each neuron, with darker colors indicating larger currents and lighter colors indicating smaller currents. **Supplementary Video 1** presents a representative laser trajectory precisely controlled using the optical board setup. Each pixel reflects the neuron's relaxation response at its spatial location. For low (high) object speed, the illuminated pixels retain stronger (weaker) residual currents when measured at the end of the light-pulse sequence, enabling the classification of both the direction and the speed of moving objects. **Supplementary Fig. 18** shows the results for motion trajectories beyond the right-diagonal direction, confirming the motion-selective capability of the proposed system.

To assess the array's motion-detection accuracy, training and inference were performed on simulated data derived from the experimental data. **Figures 3e**, **3f**, and **3g** present the relaxation time constants extracted from the measured current responses for objects moving in eight directions at the fast, medium, and slow speeds, respectively. For each speed condition, relaxation time constants were obtained from ten repeated trials for all motion directions. The measured relaxation values for each direction were flattened into a 16 × 1 column vector and fed to a neural network with 16 input neurons and 24 output neurons. Each output neuron label corresponds to a combination of motion direction and speed, such as an upright direction at slow speed. To more accurately classify single-object movement, the neural network was trained by incorporating experimental current variations into the 16-dimensional vectorized input patterns associated with each output neuron index[33,34].

During the training phase, synaptic weights were randomly initialized and optimized through iterative updates to classify 16-dimensional input vectors into 24 output neuron labels. **Figure 3h** shows clear diagonal patterns in the confusion matrix, with 24 labels corresponding to the combination of direction and speed. **Supplementary Fig. 19** shows that the test accuracy saturates at 96.7% after 80 epochs when selecting the highest output neuron. These results demonstrate that the arbitrary directions and speeds of the vectorized inputs can be clearly distinguished, even in the presence of noise induced by scattered light from moving objects. **Supplementary Video 2** shows the effect of laser crosstalk on adjacent neuron devices caused by scattered laser illumination.

Spatiotemporal multiple object detection of the KTH motion dataset

The performance of the memristive motion-streak neuron was further evaluated through simulation of the KTH motion dataset, which features multiple objects moving in different directions and at different speeds. In this study, outdoor scenarios featuring human subjects running, jogging, and walking were selected from the KTH dataset[15,16] to ensure clear separation of speeds among objects.

Figure 4a illustrates the construction of three arbitrary visual scenarios by combining two objects, eight motion directions, and three different speeds of 1 ms, 2 ms and 3 ms per pixel. For each combined scenario, four sequential motion events were applied. **Figure 4b** shows that the current responses obtained after processing three motion scenarios on a 100 × 75 pixel array were vectorized into 7500 × 1 representations and subsequently classified using a neural network with 7500 input neurons and 48 output neurons. Here, each of the 48 output neuron labels corresponds to a unique combination of object identity, motion direction, and speed, such as object 1 moving in the up-right direction at a fast speed.

Figure 4c presents the processing results for three arbitrary visual scenarios. Due to the dynamic relaxation behavior of the memristive neurons, distinct motion streaks emerge depending on both the direction and speed of each object. Slower (faster)-moving objects in scenario 3 (1) produce motion trails with longer (shorter) streaks having higher (lower) intensity. The 7500 × 1 vectorized representations of the current responses, obtained for each scenario, are also shown in the right panel.

Supplementary Fig. 20 presents the output vectors (7500 × 1) derived from motion-streak neuron responses across three visual scenarios, shown for both frame-based and static relaxation–based cases to enable direct comparison. All scenarios inherently reflect device-to-device variations and relaxation dynamics, and each vector exhibits a unique pattern that enables classification into one of the 48 output neurons.

Figure 4d shows the distributions of synaptic weights before and after training. Initially, all weights were randomly initialized. However, after training, distinct weight patterns emerged for each output neuron, indicating that the network feasibly captured discriminative features associated with different motion streak patterns. Also, **Supplementary Fig. 21** shows the learned weight distributions across output neuron indices after training for the frame-based and static relaxation–based processing approaches.

Figure 4e shows the inferred output neuron indices for the three vectorized scenarios, accurately identifying specific labels. **Figure 4f** compares inference accuracy across scenarios containing a single visual event (scenario 1), two combined events (scenarios 1 and 2), and all three visual scenarios. Consistent classification performance confirms that the proposed system maintains reliable inference even as the number of motion events increases. In contrast, conventional frame-based sensors fail to capture continuous temporal dynamics within a single scene. Phototransistors with static relaxation characteristics were reported to partially address this limitation by reflecting dynamic changes in visual scenes[8,35]. However, speed information could not be incorporated because relaxation behavior was not tunable. **Supplementary Fig. 22** shows the classification outcomes for three arbitrary visual scenarios using frame-based and static relaxation–based processing. Therefore, the capability to detect individual actions demonstrates the suitability of the proposed system for classifying different actions. **Supplementary Fig. 23** presents a confusion matrix for multiple moving-object classification, demonstrating high accuracy across the conditions.

Figure 4g compares the output neuron index classifications obtained using frame–based, static relaxation–based, and dynamic relaxation–based approaches. Frame–based sensing fails to capture temporal continuity, resulting in a low mean classification accuracy of only 12.5%. Static relaxation–based sensing partially reflects motion direction but cannot encode speed-dependent variations, resulting in a mean accuracy of 38.1%. In contrast, the dynamic relaxation–based approach enables clear separation of output neuron indices, achieving a substantially higher mean accuracy of 96.2%. The classification performance of the proposed neurons can be affected by device-level variations, so classification accuracy was assessed as a function of the relaxation time coefficient of variation (CoV). The measured cycle-to-cycle and device-to-device CoVs were 0.09 and 0.07, respectively, yielding a total CoV of 0.12. As shown in **Supplementary Fig. 24**, the test accuracy remains stable with increasing CoV, indicating that variations in motion-streak neurons do not significantly affect final classification performance.

Integrated motion streak neuron and R-C kernel for arbitrary complex movement classification of multiple-objects

To classify more complex movements involving multiple objects, detecting the temporal intervals between optical input sequences is also necessary. **Figure 5a** illustrates multiple-object scenarios with complex motion that extend beyond the simple scenarios used to evaluate arbitrary linear motion. For example, a movement in which an object first moves to the right and then moves to the left can be represented as a combination of right and left directions, while a movement that proceeds along the right diagonal after the left diagonal can be expressed as a combination of up-left and up-right directions. However, motion-streak neurons cannot distinguish such complex sequential motions. In this case, the implications of the various output vectors could be further enhanced by utilizing a physical kernel, such as the R–C kernel[36,37], which nonlinearly transforms the input vectors into kernel vectors. These kernel vectors can then be combined with the input vectors to enhance classification accuracy.

Figure 5b shows the structure of the readout layer designed to classify object identity, complex movement, and speed. In this configuration, optical input sequences applied to a 100 × 75-pixel region determine the values of the motion-streak neuron vectors and the R–C kernel vectors. These two vectors are flattened and concatenated to form a 100 × 75 × 2 input tensor. The 384 output neuron labels are defined by the combination of two object identities, eight motion directions 1 and 2, and three speeds.

Figure 5c presents the circuit diagram of the integrated motion-streak neuron and R–C kernel when applying a 4 V bias voltage, using a 1 MΩ resistor and a 500 pF capacitor to classify the given complex scenarios. Here, the motion-streak neuron modulates the length of the motion trail according to the length of the optical input, while the R–C kernel detects the interval between two optical input sequences. Longer intervals charge the capacitor more, leading to a higher voltage distribution upon subsequent optical inputs, thereby detecting the interval between consecutive sequences[38].

Figure 5d shows the processed motion-streak and kernel vectors for two representative complex movement scenarios. When each result is vectorized to 7500 × 1, the kernel vectors capture distinct features relative to the motion streak vectors. This performance is due to the varying intervals between optical sequences across pixels, resulting in unique vectors when the voltage distribution induced by the final optical input is measured. Based on these characteristics, recognition performance for complex movements was evaluated using both vectors jointly and individually.

Figure 5e presents test accuracy as a function of training epoch for three cases of vectorized inputs. The green curve corresponds to using the motion streak vector alone, yielding a low accuracy of 23.7% because it cannot process input sequences. Also, the decay of relaxation dynamics limits the ability to preserve motion history over the long term. In contrast, using the kernel vector alone yields 54.2% accuracy in recognizing complex movements. It reflects the intervals between optical sequences, but it cannot capture speed-dependent motion trails. When both vectors are used simultaneously, information on object identity, complex movement, and speed is encoded through a unique combination, resulting in a high accuracy of 91.1%. **Supplementary Fig. 25** shows the distributions of the visualized weights before and after training based on these vectors.

Figure 5f shows the predicted output neuron indices for three arbitrary scenarios based on the combined processed vectors, confirming that the activated output neurons correctly infer the ground truth. **Supplementary Fig. 26** shows the confusion matrix comparing the 384 true labels with the predicted labels. Lastly, **Figure 5g** presents the recognition accuracy of the three vectorized input cases as scenarios are cumulatively added. Across all scenario combinations, using both vectors consistently produces higher accuracy than using either vector alone.

Conclusion

This work demonstrates that a memristive motion-streak neuron intrinsically encodes spatiotemporal information through the serial integration of an Al/InGaZnO/Al optomemristor and an Ag/HfO_2/Pt volatile dynamic memristor. This integration enables simultaneous recognition of the object direction, position, and speed within a single neuromorphic system. The implemented hardware comprised a 4 × 4 motion-streak neuron array for single-object detection, achieving 96.7% accuracy. The system achieves 96.2% accuracy in identifying the positions, directions, and velocities of multiple moving objects in a simulation of the KTH dataset. Additionally, integration with an R–C kernel enables temporal interval processing, achieving 91.1% accuracy and allowing the classification of more complex motion sequences within the same hardware architecture. **Table 1** compares this work with previously reported memristive motion-detection sensors. Earlier studies processed only optical inputs and performed single-object detection on simple datasets[8,39]. In contrast, this work enables multiple-object detection on a complex video dataset using an integrated device-array structure, achieving accuracy comparable to that of the software solution. (**Supplementary Fig. 27**).

Methods

Device Fabrication

For the Al/IGZO/Al optomemristor, a SiO_2 layer was thermally grown on the p-type (100) Si wafer as a starting substrate. Then, an IGZO active layer was deposited by RF sputtering. The IGZO layer was patterned through photolithography and dry etching. A 50-nm-thick Al electrode layer and a 50-nm-thick Pt passivation layer were deposited using an electron beam evaporator, followed by the lift-off process. A line cell structure was designed to maximize the light-receiving area.

The top electrode of the Ag/HfO_2/Pt dynamic memristor was connected via the right metal Al electrode of the Al/IGZO/Al optomemristor, and the details of the fabrication process are described elsewhere[41,42]. A 50-nm-thick Pt bottom electrode metal layer was deposited by electron-beam evaporation and patterned by photolithography and lift-off. Then, an 8-nm-thick HfO_2 switching layer was deposited through thermal atomic layer deposition at a substrate temperature of 250 °C. The precursor for Hf and oxidizer were tetrakis (dimethylamido) hafnium and O_3, respectively. The HfO_2 layer was patterned by

photolithography and dry etching of the bottom Pt metal electrode of the dynamic memristor and the right metal Al electrode of the optomemristor for pad contact. Finally, a 70-nm-thick Ag top electrode layer and a 50-nm-thick Pt passivation layer were deposited using a thermal evaporator and an electron-beam evaporator, respectively, and patterned by photolithography and lift-off. **Supplementary Fig. 10** illustrates the detailed process flow of the integrated motion streak neuron.

Optical Measurements

A custom optical measurement system was constructed to quantify the spatiotemporal response of the 4 × 4 wire-bonded motion-streak neuron arrays. **Figure 3a** represents the schematic of the optical board setup. The optical path was aligned using a 4 × 4 laser array comprising 532 nm green laser diodes with a light intensity of 12.35 mW/cm^2 (Q-LINE). Each laser diode was fixed to a laser diode mount (Q-LINE), and the light was aligned using mirror mounts (Startnow) with 25 mm Si reflective mirrors (FONLAND). The optical modules were assembled on an aluminum optical board (AUTOMATION PARTS, PL23) to ensure stable multilayer beam alignment. The reflected laser beams from the multilayer modules were focused onto the motion-streak neuron devices (devices under test, DUTs) located at the focal plane.

For synchronized optical illumination and electrical readout, a microcontroller unit (STM32, STMicroelectronics) was connected to each laser channel via bipolar junction transistors (2N2222). The microcontroller unit (MCU) was interfaced with a control computer via a general purpose interface bus (GPIB) cable, enabling optical pulse generation in response to a control-voltage waveform. Through the same GPIB interface, the pulse generator triggered the readout-voltage window, while the MCU switched the transistor within this window to precisely control the illumination pulse width and to perform automated timing control and data acquisition. Relaxation currents were measured simultaneously using multiple oscilloscope channels connected to the bonded pads of each device, allowing parallel acquisition of spatiotemporal responses. **Supplementary Fig. 16** shows the actual hardware configuration used to detect light in different directions.

Electrical Measurements

The DC *I*–*V* characteristics were measured using the semiconductor parameter analyzer (4155A, Hewlett-Packard). An Agilent 8110A pulse generator and oscilloscope (TDS 684C, Tektronix) were used for the pulse measurements. White-light illumination was provided by a pulse-width modulator (ZK-PP2K dual-mode pulse driver) and a light-emitting-diode (LED) lamp module (XML-T6 5W LED module).

Movement Classification Methods (single object and multiple objects using the KTH dataset)

For the single-object case, a neural network with a size of 16 × 24 was trained on 240 experimentally measured responses from the reflective optics assembly, divided into 144 training datasets and 96 test sets. To generate customized datasets from the KTH motion dataset, action sequences were constructed by combining two objects, eight motion directions, and three speeds, and were then resized from the original resolution of 160 × 120 pixels to 100 × 75 pixels. To train arbitrary scenarios involving

multiple objects, a neural network with a structure of 7500 × 48 and 15000 × 384 was trained using the training sets and test sets ratio of 8:2. In both systems, backpropagation was used for the training and testing processes, and the Adam optimizer was applied to minimize the cost function in the Python package PyTorch.

Declarations

Code Availability

The code supporting the simulation in this Article is available from the corresponding author upon reasonable request.

Acknowledgements

H.J. Park, J.H. Kim and H.W. Kim contributed equally to this work. This work was supported by the National Research Foundation of Korea (2021R1A3B2079882).

References

1. L. Mennel, J. Symonowicz, S. Wachter, D. K. Polyushkin, A. J. Molina-Mendoza, T. Mueller, *Nature***579**, 62 (2020).
2. H. Jang, H. Hinton, W.-B. Jung, M.-H. Lee, C. Kim, M. Park, S.-K. Lee, S. Park, D. Ham, *Nat. Electron.***5**, 519 (2022).
3. Y. Chai, *Nature***579**, 32 (2020).
4. C. Choi, J. Leem, M. Kim, A. Taqieddin, C. Cho, K. W. Cho, G. J. Lee, H. Seung, H. J. Bae, Y. M. Song, *Nat. Commun.* **11**, 5934 (2020).
5. K. Simonyan, A. Zisserman, *Adv. Neural Inf. Process Syst.***1**, 568-576 (2014).
6. F. Zhou, Y. Chai, *Nat. Electron.***3**, 664 (2020).
7. X. Li, J. Tang, Q. Zhang, B. Gao, J. J. Yang, S. Song, W. Wu, W. Zhang, P. Yao, N. Deng, *Nat. Nanotechnol.***15**, 776 (2020).
8. J. Chen, Z. Zhou, B. J. Kim, Y. Zhou, Z. Wang, T. Wan, J. Yan, J. Kang, J.-H. Ahn, Y. Chai, *Nat. Nanotechnol.***18**, 882 (2023).
9. M. Irani, P. al Anandan, J. Bergen, R. Kumar, S. Hsu, *Signal Process. Image Commun.***8**, 327 (1996).
10. J. E. Dowling, *The Retina: An Approachable Part of the Brain*, Harvard University Press (1987).
11. A. London, I. Benhar, M. Schwartz, *Nat. Rev. Neurol***9**, 44 (2013).
12. C. H. Anderson, D. C. Van Essen, J. L. Gallant (1990).
13. M. Morgan, S. Benton, *Nature***340**, 385 (1989).
14. W. S. Geisler, *Nature***400**, 65 (1999).

15. P. Antonik, N. Marsal, D. Brunner, D. Rontani, *Nat. Mach. Intell.***1**, 530 (2019).
16. S. Xu, J. Wang, S. Yi, W. Zou, *Nat. Commun.***13**, 7970 (2022).
17. D. Apthorp, D. S. Schwarzkopf, C. Kaul, B. Bahrami, D. Alais, G. Rees, *Proc. R. Soc. B.***280**, 20122339 (2013).
18. M. Tohmi, S. Tanabe, J. Cang, *Cell reports***34**, 108617 (2021).
19. L. Hu, J. Yang, J. Wang, P. Cheng, L. O. Chua, F. Zhuge, *Adv. Funct. Mater.***31**, 2005582 (2021).
20. M. A. Arbib, *The Handbook of Brain Theory and Neural Networks*, MIT Press (2003).
21. W. Wang, M. Wang, E. Ambrosi, A. Bricalli, M. Laudato, Z. Sun, X. Chen, D. Ielmini, *Nat. Commun.***10**, 81 (2019).
22. K. S. Woo, J. Kim, J. Han, J. M. Choi, W. Kim, C. S. Hwang, *Adv. Intell. Syst.***3**, 2100062 (2021).
23. K. S. Woo, J. Kim, J. Han, W. Kim, Y. H. Jang, C. S. Hwang, *Nat. Commun.***13**, 5762 (2022).
24. K. S. Woo, J. Han, S. Yi, L. Thomas, H. Park, S. Kumar, C. S. Hwang, *Nat. Commun.***15**, 3245 (2024).
25. K. S. Woo, H. Park, N. Ghenzi, A. A. Talin, T. Jeong, J.-H. Choi, S. Oh, Y. H. Jang, J. Han, R. S. Williams, S. Kumar, C. S. Hwang, *ACS Nano***18**, 17007 (2024).
26. B. R. Tak, V. Gupta, A. K. Kapoor, Y.-H. Chu, R. Singh, *ACS Appl. Mater. Interfaces.***1**, 2463 (2019).
27. M. Hussain, A. Ali, S. H. A. Jaffery, S. Aftab, S. Abbas, M. Riaz, T. P. A. Bach, M. Raza, J. Iqbal, S. Hussain, *Nanoscale***14**, 10910 (2022).
28. Y. Liao, Y. J. Kim, M. Kim, *J. Chem. Eng.***476**, 146838 (2023).
29. Y. Zhou, J. Fu, Z. Chen, F. Zhuge, Y. Wang, J. Yan, S. Ma, L. Xu, H. Yuan, M. Chan, X. Miao, Y. He, Y. Chai, *Nat. Electron.***6**, 870 (2023).
30. H. Shao, Y. Ji, R. Wang, J. Liu, Y. Li, B. Liu, W. Li, Y. Xie, L. Xie, J. C. Ho, *Nano Energy***130**, 110133 (2024).
31. H. Fang, S. Ma, J. Wang, L. Zhao, F. Nie, X. Ma, W. Lü, S. Yan, L. Zheng, *Adv. Funct. Mater.***34**, 2409045 (2024).
32. C. Lu, J. Meng, J. Song, K. Xu, T. Wang, H. Zhu, Q. Sun, D. W. Zhang, L. Chen, *ACS Nano***18**, 29715 (2024).
33. S. Seo, B.-S. Kang, J.-J. Lee, H.-J. Ryu, S. Kim, H. Kim, S. Oh, J. Shim, K. Heo, S. Oh, *Nat. Commun.***11**, 3936 (2020).
34. Y. Li, Z. Xuan, J. Lu, Z. Wang, X. Zhang, Z. Wu, Y. Wang, H. Xu, C. Dou, Y. Kang, *Adv. Funct. Mater.***31**, 2100042 (2021).
35. R. Wang, S. Wang, K. Liang, Y. Xin, F. Li, Y. Cao, J. Lv, Q. Liang, Y. Peng, B. Zhu, *Small***18**, 2201111 (2022).
36. Y. H. Jang, W. H. Kim, J. H. Kim, K. S. Woo, H. J. Lee, J. W. Jeon, S. K. Shim, J. Han, C. S. Hwang, *Nat. Commun.***12**, 5727 (2021).
37. S. K. Shim, Y. H. Jang, J. Han, J. W. Jeon, D. H. Shin, Y. R. Kim, J.-K. Han, K. S. Woo, S. H. Lee, S. Cheong, J. Kim, H. Seo, J. Shin, C. S. Hwang, *Small***20**, 2306585 (2024).

38. S. K. Shim, K. Lee, J. Han, D. H. Shin, S. H. Lee, S. Cheong, Y. H. Jang, C. S. Hwang, *Adv. Mater.***36**, 2410432 (2024).
39. Y. Sun, Q. Li, X. Zhu, C. Liao, Y. Wang, Z. Li, S. Liu, H. Xu, W. Wang, *Adv. Intell. Syst.***5**, 2200196 (2023).
40. H. Song, M. G. Lee, G. Kim, D. H. Kim, G. Kim, W. Park, H. Rhee, J. H. In, K. M. Kim, *Adv. Mater.***36**, 2309708 (2024).
41. J. H. Kim, H. W. Kim, M. J. Chung, D. H. Shin, Y. R. Kim, J. Kim, Y. H. Jang, S. W. Cheong, S. H. Lee, J. Han, H. J. Park, J. Han, C. S. Hwang, *Nanoscale Horiz.*, **9**, 2248-2258 (2024).
42. H. W. Kim, J. H. Kim, D. H. Shin, M. J. Chung, T. W. Park, H. J. Park, J. Han, C. S. Hwang, *Adv. Mater.*, e13907 (2025).

Figures

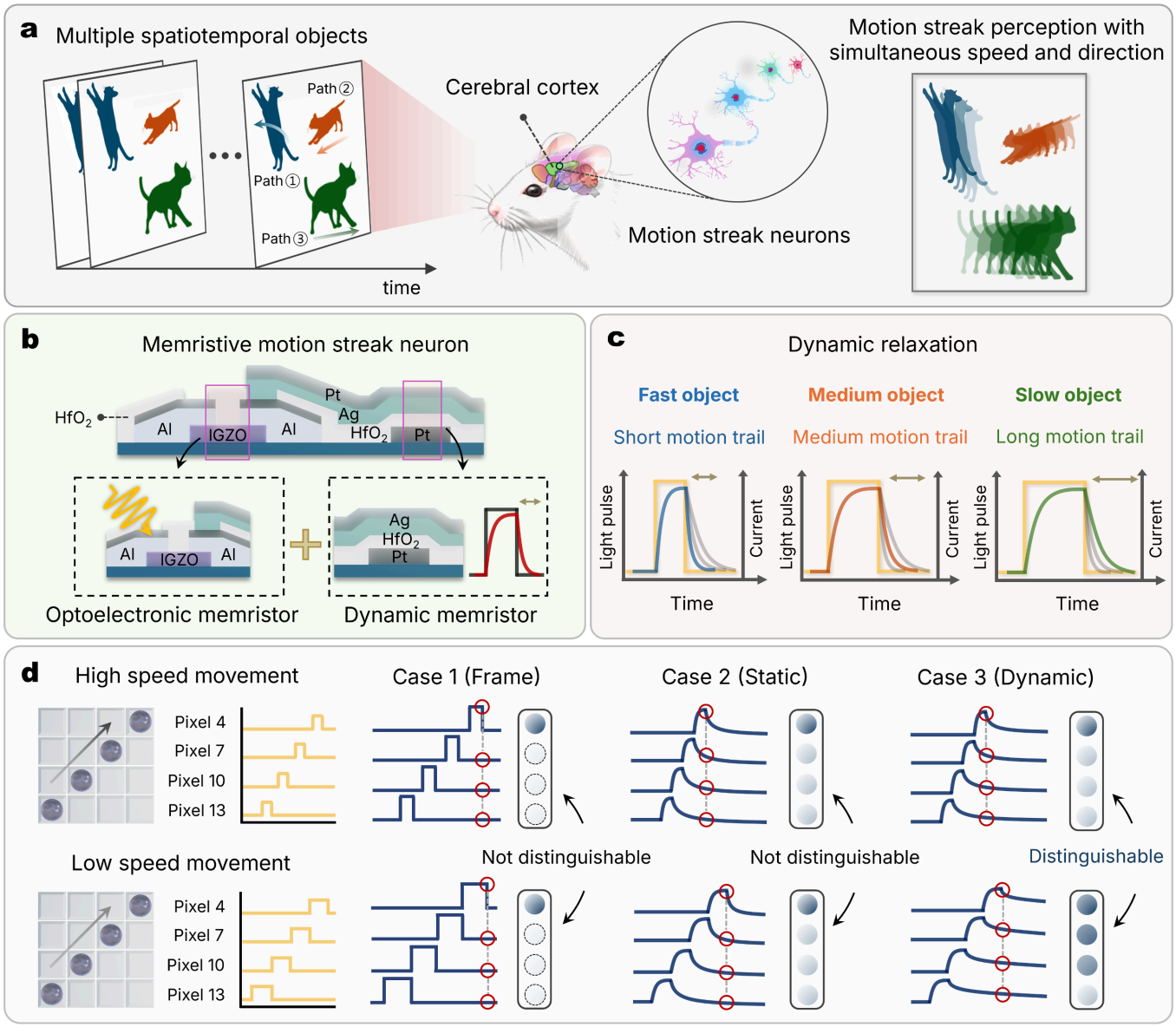

Figure 1

Illustration of a motion streak neuron for spatiotemporal multiple object detection.

(a) Biological motion streak neurons in a mouse cerebral cortex. Motion-streak neurons are featured in simultaneously recognizing the speed and direction of multiple objects. (b) A motion streak neuron device consisting of an Al/IGZO/Al optoelectronic memristor and an Ag/HfO_2/Pt dynamic memristor. The optoelectronic memristor converts external optical stimuli into electrical currents, and the dynamic memristor exhibits relaxation characteristics that encode object velocity as motion streaks. (c) The relaxation time of the memristive motion streak neuron increases with the input pulse width. When the integrated device directly receives light, generated motion trails can capture the speed characteristics of multiple objects. (d) By encoding the object presence time into the optical pulse width, motion streaks can be clearly distinguished through dynamic relaxation. In contrast, frame-based approaches without relaxation dynamics and static approaches lacking temporal correlation cannot distinguish velocity-dependent features.

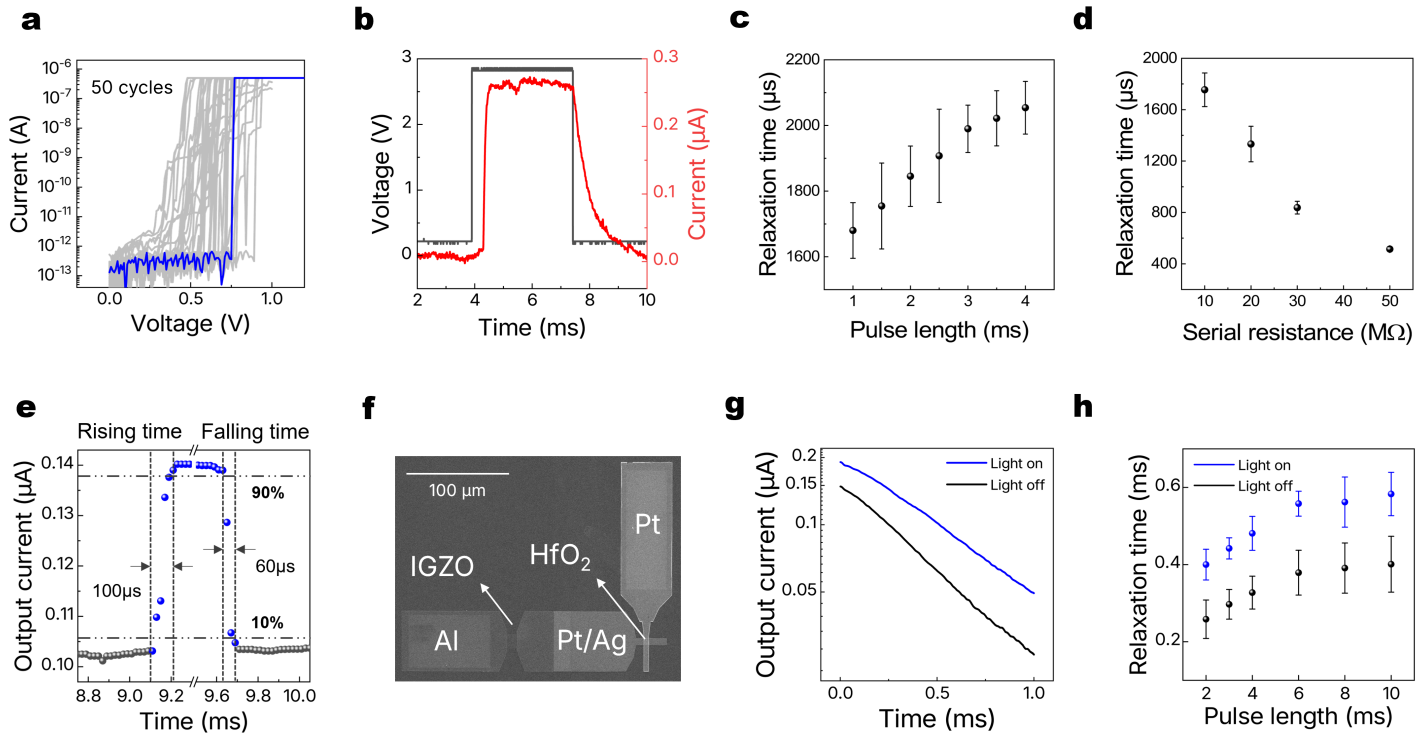

Figure 2

Electrical and optical properties of the Ag/HfO_2/Pt dynamic memristor, Al/IGZO/Al optomemristor and the integrated device.

(a) DC current-voltage (*I-V*) characteristics of the dynamic memristor. (b) Threshold switching behavior of the dynamic memristor under an input pulse of 2.8 V over 2.5 ms. The output current (red) shows the threshold switching behavior with relaxation dynamics. (c) Relaxation time at varying pulse widths under

a fixed pulse voltage of 2.8 V and a load resistance of 10 MΩ, and (d) Relaxation behaviors at different series resistances under a fixed pulse condition (2.8 V and 2.5 ms). (e) Switching behavior of the optomemristor for incident light under a fixed voltage of 2.8 V. Rising and falling times are 100 μs and 60 μs, respectively. (f) Scanning electron microscopy image of the integrated device composed of the optomemristor and the dynamic memristor. (g) Relaxation behavior of the integrated motion streak neuron at different light conditions, with a fixed pulse condition (4 V and 8 ms), (h) relaxation time of the integrated motion streak neuron at different pulse widths and light conditions, with a fixed pulse amplitude of 4 V.

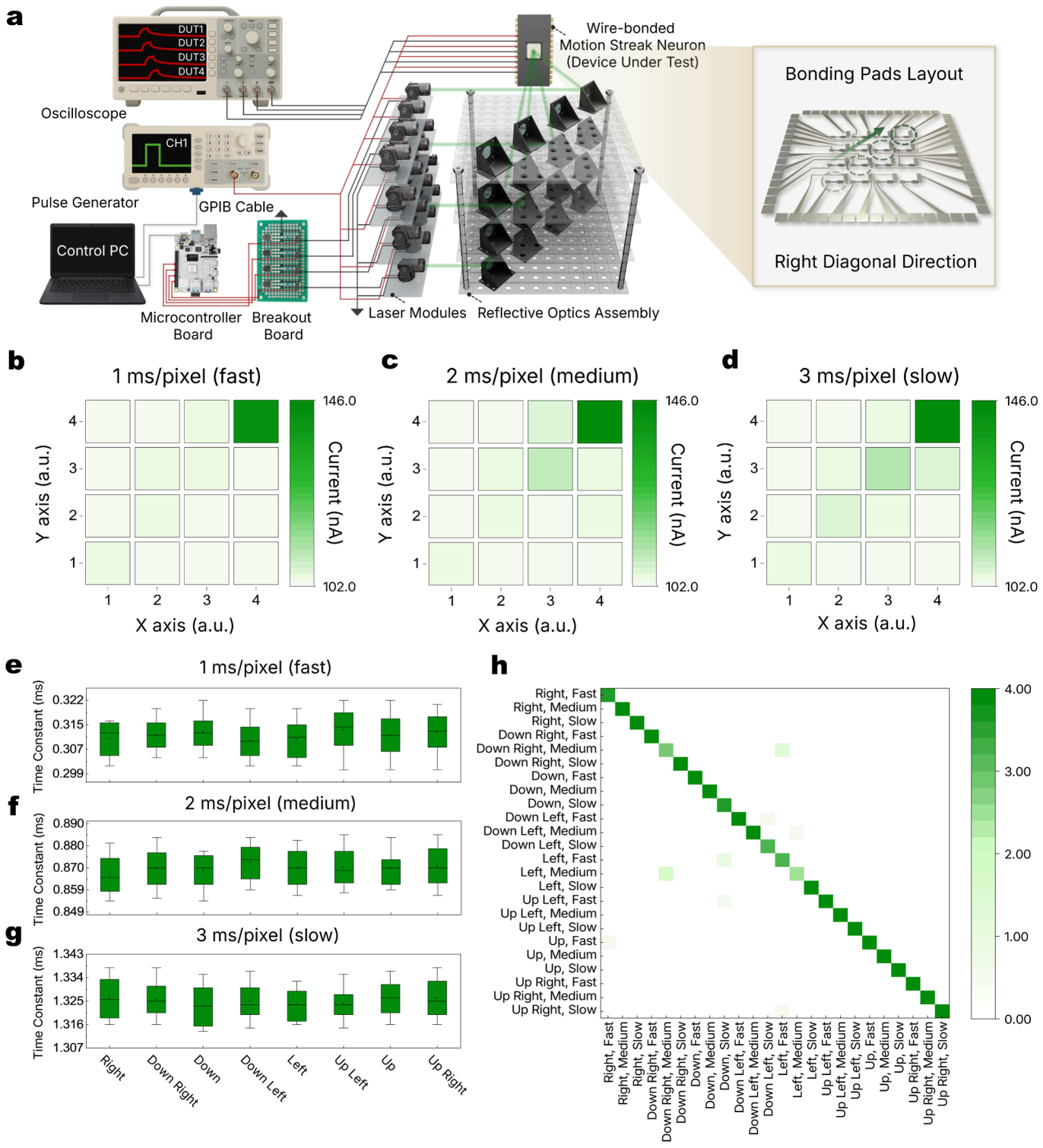

Figure 3

Hardware demonstration of motion streak neurons for single object movement classification.

(a) Optical setup for precise timing control of the optical and electrical stimuli of the motion-streak neuron hardware. The enlarged image on the right shows the layout of the 4 × 4 wire-bonded motion-streak neuron array, illustrating the application of light pulses along the right-diagonal direction.

Experimentally measured current of an object moving toward the right diagonal direction at different speeds: (b) fast (1 ms per pixel), (c) medium (2 ms per pixel), and (d) slow (3 ms per pixel). Relaxation time constants extracted from the measured current responses for objects moving in eight different directions, including vertical, horizontal, and diagonal trajectories: (e) fast (1 ms per pixel), (f) medium (2 ms per pixel), and (g) slow (3 ms per pixel). Each directional condition was measured over ten repeated trials. (h) Confusion matrix for single-object movement classification.

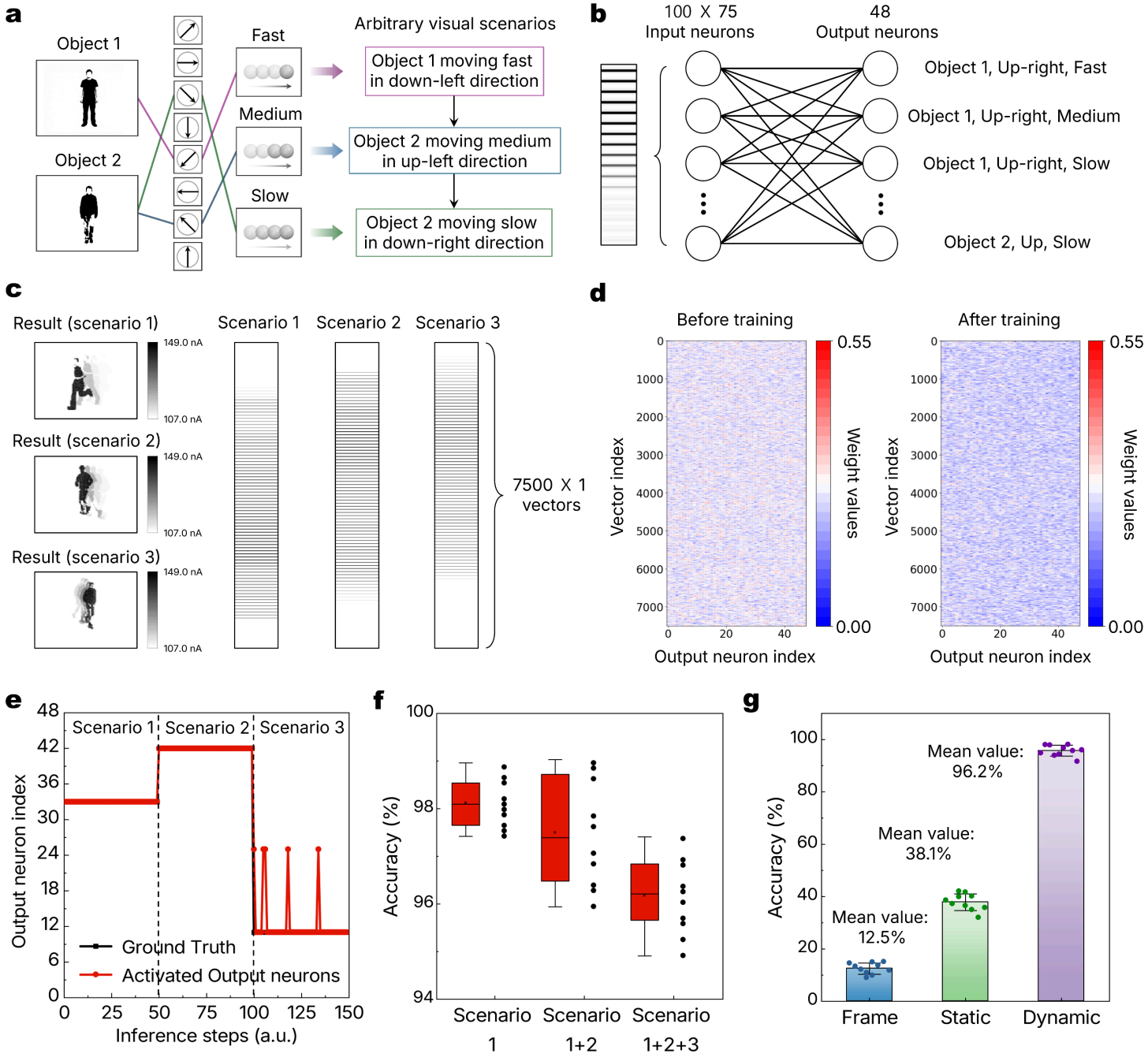

Figure 4

Spatiotemporal multiple object detection of the KTH motion dataset.

(a) Arbitrary visual scenarios were constructed by combining two objects, eight motion directions, and three different speeds. Four sequential motion events were applied consecutively. (b) After each motion event, the measured current responses from a 100 × 75 pixels were vectorized into a 7500 × 1 size and processed by a neural network composed of 7500 input neurons and 48 output neurons for classification. (c) Processed results for three arbitrary visual scenarios. Distinct motion streaks were formed depending on each motion event, and the results were transformed to 7500 × 1 vectors. (d) Visualization of the neural network weight distributions before and after training. (e) Inference results of the output neuron indices for the three vectorized scenarios using the trained weights. (f) Inference results of the output neuron indices for accumulated scenarios containing one, two, and three visual scenarios. (g) Comparison of output neuron index classifications obtained using frame-based, static, and dynamic approaches. Unlike the dynamic approach that distinct motion streaks enable clear index separation, the frame-based and static approaches fail to resolve the output neuron indices.

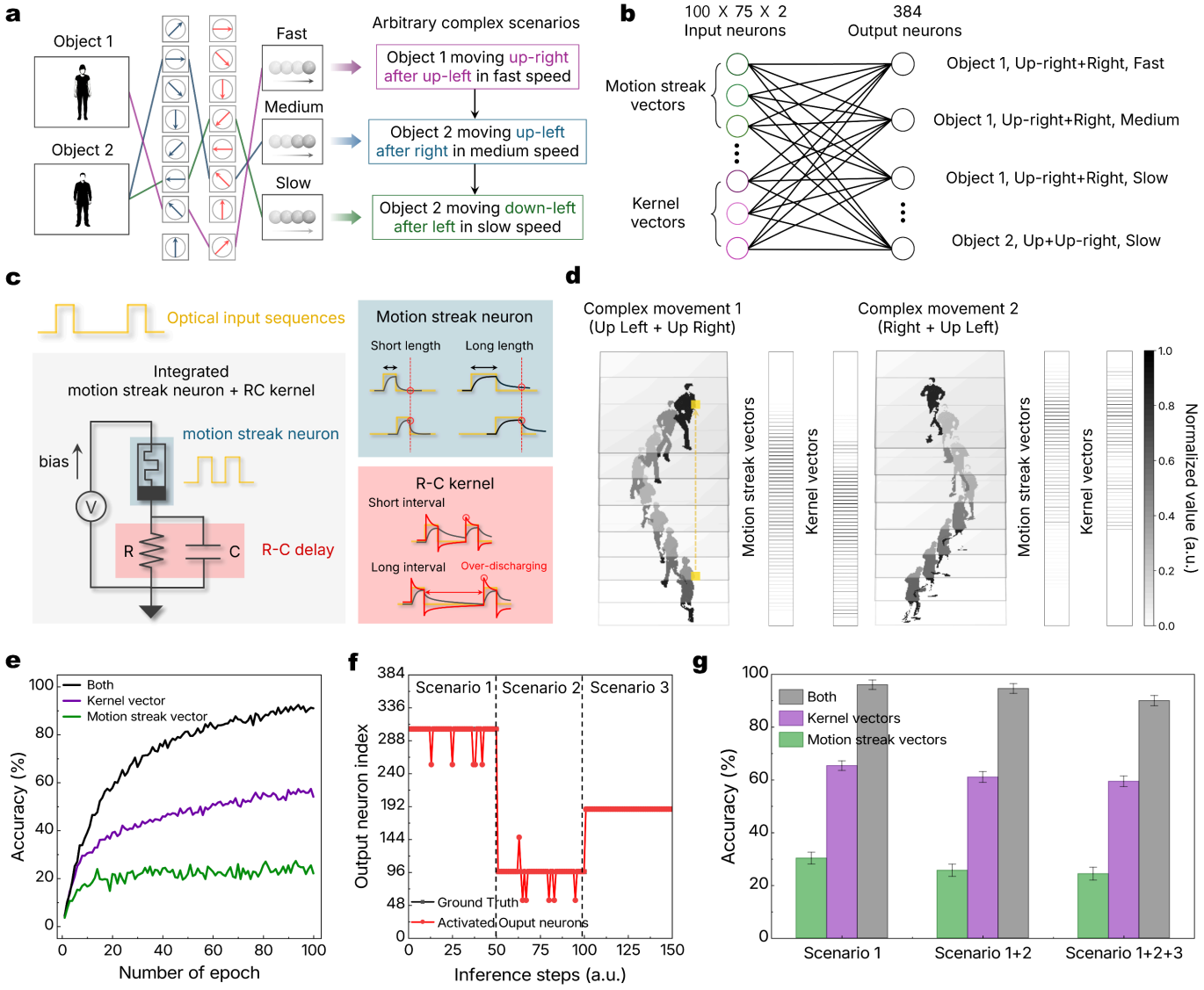

Figure 5

Integrated motion streak neuron and R-C kernel for arbitrary complex movement classification of multiple objects.

(a) Arbitrary complex scenarios were constructed by combining two objects, dual trajectories with eight motion directions, and three different speeds. (b) After complex movement scenarios, the motion streak vectors and R-C kernel vectors from a 100 × 75 pixels were vectorized into a 15000 × 1 size and processed by a neural network composed of 15000 input neurons and 384 output neurons for classification. (c) Circuit diagram of the integrated motion streak neuron and R–C kernel. The motion-streak neuron produces a motion trail proportional to the optical pulse width, and the R–C kernel encodes the temporal intervals in complex motion patterns. (d) Processed results for three arbitrary complex scenarios. Two vectors were formed independently depending on the complex motion events. (e) Test accuracy as a function of epochs for three vectorized input cases. Compared with cases using the motion streak vector or the kernel vector alone, combined vectors represent significantly higher classification accuracy. (f) Inference results of the output neuron indices for the three vectorized inputs with motion streak vectors and R-C kernel vectors. (g) Comparison of test accuracy across three vectorized input cases under accumulated scenarios comprising one, two, and three complex visual events.

Supplementary Files

This is a list of supplementary files associated with this preprint. Click to download.

- SupportingInformation.docx
- SupplementaryVideo1.mp4
- SupplementaryVideo2.mp4